Regioisomeric Effects of Donor–Acceptor–Acceptor′ Small-Molecule Donors on the Open Circuit Voltage of Organic Photovoltaics

Xiaozhou Che, Chin-Lung Chung, Xiao Liu, Shu-Hua Chou, Yi-Hung Liu, Ken-Tsung Wong, and Stephen R. Forrest**

Organic photovoltaic (OPV) cells have been widely studied for transforming solar energy to electric current. Compared to typical Si-based photovoltaics, OPVs have advantages such as potentially low cost, light weight, and flexibility. Among various organic materials, small molecules are particularly attractive for this purpose since they can be highly purified and deposited by vapor phase techniques.[1–5] Often, small-molecule donors have symmetric structures with zero ground-state dipole moments such as many squaraines and tetraphenyldibenzoperiflanthene (DBP).[6–9] Recently, a class of molecules bearing both an electron-donating (d) and two electron-accepting (a, a′) functional groups configured in a d–a–a′ structure have been used in high-efficiency OPVs.[10–12] These structural motifs are interesting in that they have large ground-state dipole moments that strongly affect their thin film morphologies. This molecular design also results in a narrow energy gap leading to absorption extending into the near-infrared (NIR) region, as well as a relatively deep highest occupied molecular orbital (HOMO) level. Such a combination of properties leads to both a high open circuit voltage (V_{OC}) and short circuit current (J_{SC}).[11] Recently, Griffith et al. reported that the intermolecular alignments governed by the large ground-state dipole moments in d–a–a′ compounds lead to efficient intermolecular charge transfer (CT) and therefore strong hole coupling and a high hopping rate between neighboring molecules. A power conversion efficiency (PCE) of 9.6 ± 0.5 % under 1 sun, AM 1.5G simulated solar illumination was thus achieved.[13] The d–a–a′ molecular configuration has also been applied to multijunction cells as NIR absorbers with PCE > 11%.[14] Lately, a group of dipolar donor molecules bearing a rigid and coplanar electron-donating dithieno[3,2-*b*:2′,3′-d]pyrrole (DTP) *d*-unit and an electron-withdrawing benzothiadiazole- or pyrimidine-dicyanovinylene as the a–a′ group has been reported.[15] In this case, the molecules with DTP donor units capped with aryl groups showed improved chemical stability as compared with unfunctionalized DTP, yielding OPVs with PCE = 5.6% when blended with C_{70} as the electron acceptor. However, the conformational flexibility between DTP and the terminal aryl substitution may subtly influence the intermolecular interactions that are crucial for OPV performance.

In this work, we synthesize and characterize a set of d–a–a′-type donor molecules to further clarify their structure–property–performance relationships in OPVs. As shown in **Figure 1**a, two asymmetric heterotetracenes with different thienyl ring arrangements are introduced to couple with benzothiadiazole-dicyanovinylene, giving the isomeric d–a–a′ structures of 2-((7-(*N*-(2-ethylhexyl)-benzothieno[3,2-*b*]thieno[2,3-*d*]-pyrrol-2-yl)benzo[*c*][1,2,5]thiadiazol-4-yl)methylene)malononitrile (antiBTDC) and 2-((7-(*N*-(2-ethylhexyl)-benzothieno[3,2-*b*]-thieno[3,2-*d*]pyrrol-2-yl)benzo[*c*][1,2,5]thiadiazol-4-yl)methylene) malononitrile (synBTDC). Compared to previously reported DTP-based molecules,[15] instead of introducing an aryl end-capping group, these d–a–a′ molecules employ a terminal benzene ring which is fused with the electron-donating DTP unit to give a coplanar structure with reduced conformational variations. We characterize these two isomers via single-crystal X-ray diffraction, density functional theory (DFT) calculations, and steady-state/transient photoluminescence (PL) to understand the regioisomeric effects[16,17] on their structural and charge transfer properties. We find that antiBTDC exhibits more compact crystal packing and higher oscillator strength of the lowest energy excitations compared to those of synBTDC, leading to stronger inter- and intramolecular charge transfer with a reduced energy gap. An OPV adopting antiBTDC mixed with C_{70} achieves J_{SC} = 14.2 ± 0.7 mA cm^{-2}, V_{OC} = 0.91 ± 0.01 V, fill factor (FF) = 0.56 ± 0.01, and PCE = 7.2 ± 0.3%. For synBTDC, the π-conjugation is interrupted by the N-bridge atom as indicated by the highlighted chemical structure shown in Figure 1a. The reduced effective conjugation length and

X. Che, Prof. S. R. Forrest
Applied Physics Program
University of Michigan
Ann Arbor, MI 48109, USA
E-mail: stevefor@umich.edu
C.-L. Chung, S.-H. Chou, Y.-H. Liu, Prof. K.-T. Wong
Department of Chemistry
National Taiwan University
Taipei 10617, Taiwan
E-mail: kenwong@ntu.edu.tw
X. Liu, Prof. S. R. Forrest
Department of Electrical Engineering and Computer Science
University of Michigan
Ann Arbor, MI 48109, USA
Prof. K.-T. Wong
Institute of Atomic and Molecular Science
Academia Sinica
Taipei 10617, Taiwan
Prof. S. R. Forrest
Department of Physics and Department of Materials Science and Engineering
University of Michigan
Ann Arbor, MI 48109, USA

DOI: 10.1002/adma.201601957

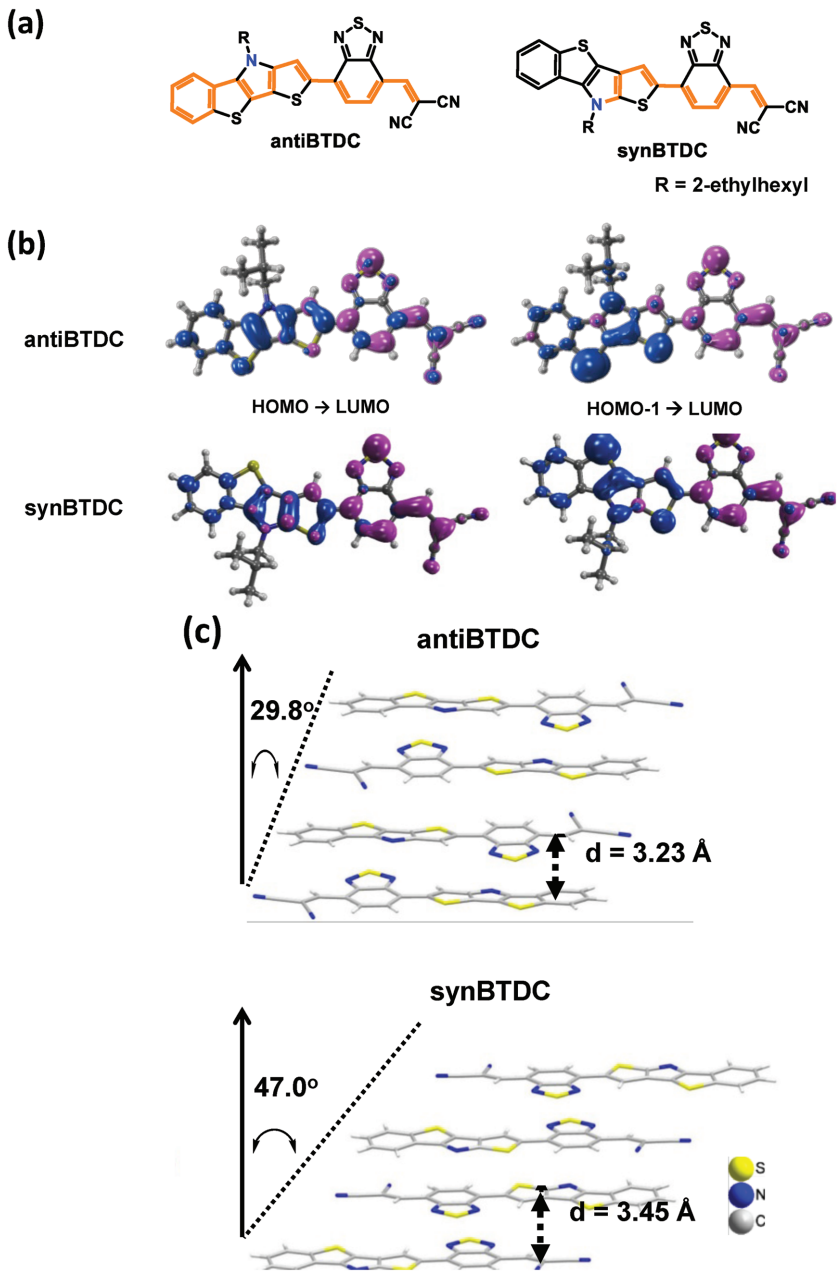

Figure 1. a) Molecular structural formulae of antiBTDC and synBTDC. b) Charge densities of the lowest energy singlet excitations ($S_1 \leftarrow S_0$) with the given molecular orbital (MO) transitions, where blue denotes occupied and purple symbolizes unoccupied MOs. c) Crystal packing configurations of antiBTDC and synBTDC. Side chains are omitted for clarity.

intramolecular charge transfer lead to a blue-shifted absorption with a lower extinction coefficient despite the presence of the electron-donating nitrogen lone pair. Nevertheless, the HOMO of synBTDC is stabilized compared to antiBTDC, leading to an increased V_{OC} = 1.01 ± 0.01 V. A third donor molecule 2-((2-(4-(2-ethylhexyl)-4H-benzothieno[3,2-*b*]thieno[2,3-*d*]pyrrol-2-yl)pyrimidin-5-yl)methylene)malononitrile (PYDC) was synthesized for comparative study. This molecule is characterized by the replacement of the central benzothiadiazole "a" unit of antiBTDC by pyrimidine with reduced quinoidal character.[18] PYDC exhibits an even larger hypsochromic shift in the absorption spectrum, yielding an OPV with the highest V_{OC} = 1.06 ± 0.01 V. Together with previously reported DTP-based d–a–a′ donors, we establish a clear correlation between molecular conjugation length and HOMO energy. Most notably, the cross-conjugation of synBTDC effectively reduces its backbone conjugation without sacrificing chemical stability and charge transport character, leading to increased V_{OC} while maintaining a comparable FF and PCE relative to that of antiBTDC.

The crystal structures of antiBTDC and synBTDC characterized by X-ray diffraction are shown in Figure S1 (Supporting Information), with the data summarized in Table S1 (Supporting Information). The bond lengths of the labeled carbon atoms are listed in Table S2 (Supporting Information). Bond length alternation (BLA) is defined as the difference between C3—C4 bond length and the average of C2—C3 and C4—C5 bond lengths of the benzothiadiazole acceptor.[19] We find that antiBTDC has a smaller BLA = 0.031 Å compared to 0.046 Å for synBTDC, as well as a decreased C1—C2 bond length.

The electronic density plots in Figure 1b can be used to predict the transition characteristics for each molecular orbital (MO) composition, with the calculated values listed in Table S3 (Supporting Information). Compared to synBTDC, a bathochromic absorption shift together with a fourfold increase in the oscillator strengths (*f*) of the lowest energy singlet ground-to-excited state transition ($S_1 \leftarrow S_0$) was found for antiBTDC. The $S_1 \leftarrow S_0$ of antiBTDC and synBTDC comprise two MO transitions (HOMO→LUMO, the lowest unoccupied molecular orbital, and HOMO-1→LUMO) with different weighting. The HOMOs are delocalized over the molecular backbone while the LUMOs are localized on the electron-deficient benzothiadiazole-dicyanovinylene fragments. The HOMO-1 is primarily populated on the electron-rich heterotetracene unit. The lowest energy transitions of antiBTDC and synBTDC comprise both π–π^* and charge transfer character. The MO spatial overlap for $S_1 \leftarrow S_0$ is calculated to be 43% and 27% for antiBTDC and synBTDC, respectively. The internal dipole moments of the ground states (μ_g) and the excited states (μ_e) are also listed in Table S3 (Supporting Information), together with the transition dipole moments (μ_{tr}) and the total dipole moments change (μ_{ge}). Both μ_g = 15.42 D and μ_e = 16.48 D of antiBTDC are slightly larger than those of synBTDC (μ_g = 14.84 D, μ_e = 13.77 D), along with the larger μ_{tr} = 5.00 D.

The large ground-state dipole moments of antiBTDC and synBTDC lead to an antiparallel molecular arrangement along

their long backbone axes, as shown by the crystal packing configurations in Figure 1c. The antiBTDC molecule has a dihedral angle of 8.8° between the thienoacene donor and benzothiadiazole acceptor with an intermolecular interfacial distance of 3.23 Å. In contrast, synBTDC shows an almost perfect coplanar conformation with a dihedral angle of 1.9° between the d and central a unit, but a larger interfacial distance of 3.45 Å. Also seen from Figure 1c, antiBTDC exhibits a co-facial π-stacking with a pitch angle of 29.8°, while synBTDC forms a staircase-like arrangement with a much larger pitch angle of 47.0°. DFT calculations were performed to visualize the electrostatic potential of monomers and dimers (Figure S2, Supporting Information) found in the crystal structure. The antiparallel dimeric pairs show a reduced polarized electrostatic potential as compared to that of the monomers. The antiBTDC dimer exhibits a more homogeneous electron density distribution over the molecular backbone as compared to the synBTDC dimer due to its compact stacking arrangement where each molecular donor unit is more closely positioned to an acceptor unit.

Figure 2a shows the molecular extinction coefficients in dichloromethane solution, and their normalized thin film absorbances. Compared with antiBTDC, the thin film absorption onset of synBTDC is hypsochromically shifted from a wavelength of $\lambda = 820$ to 750 nm. The full width at half maxima (FWHM) of the absorption spectra of both films are broadened by ≈70 nm with a 10 nm red shift compared with their solution spectra. Compared with antiBTDC, the optical energy gap of synBTDC is increased from 1.52 ± 0.03 to 1.66 ± 0.04 eV, while the measured HOMO level is shifted from −5.4 ± 0.05 to −5.5 ± 0.05 eV.

The detailed photophysical and electrochemical parameters of these two donors are summarized in Table S4 (Supporting Information). They exhibit relatively high thermal stability with decomposition temperatures (i.e., the temperature corresponding to 5% weight loss) of 331 and 319 °C, respectively, as determined by thermogravimetric analysis. Both of the donor molecules show remarkable electrochemical stability as probed by cyclic voltammetry (Figure S3, Supporting Information). Also, the vacuum deposited antiBTDC and synBTDC films have similar hole mobilities of $3 \pm 2 \times 10^{-6}$ cm^2 V^{-1} s^{-1} measured by metal insulator semiconductor–charge extraction by linearly increasing voltage (MIS-CELIV);[20,21] see Figure S4a,b (Supporting Information). The space charge limited current (SCLC) measurement of these two donors is then used to fit the trap density of states (N_t) from the trap limited current and the conductivity (σ) obtained from the ohmic regime (Figure S4c, Supporting Information). The neat antiBTDC and synBTDC show similar $N_t \approx 8 \times 10^{18}$ and 1×10^{19} cm^{-3}, respectively, while antiBTDC has more than one order of magnitude higher conductivity ($\sigma \approx 5 \times 10^{-8}$ S cm^{-1}) than synBTDC ($\sigma \approx 2 \times 10^{-9}$ S cm^{-1}).

To examine the photovoltaic performance of the two regioisomeric donors, we mixed them with C_{70} to form the active layer of the vacuum deposited OPV cells. The optimized device structure as shown in Figure 2b, inset, is configured as follows: ITO/MoO_3 (10 nm)/d–a–a′ donor:C_{70} (1:2 ratio by vol.)/bathophenanthroline (BPhen):C_{60} (1:1 ratio by vol., 10 nm)/BPhen (5 nm)/Ag (100 nm). Here, MoO_3 serves as the anode buffer due to its high optical transmittance, electron conductivity, and work function.[22] The transparent exciton blocking and electron conducting buffer consists of a BPhen:C_{60} (1:1) mixed layer capped with a neat BPhen layer adjacent to the cathode.[23]

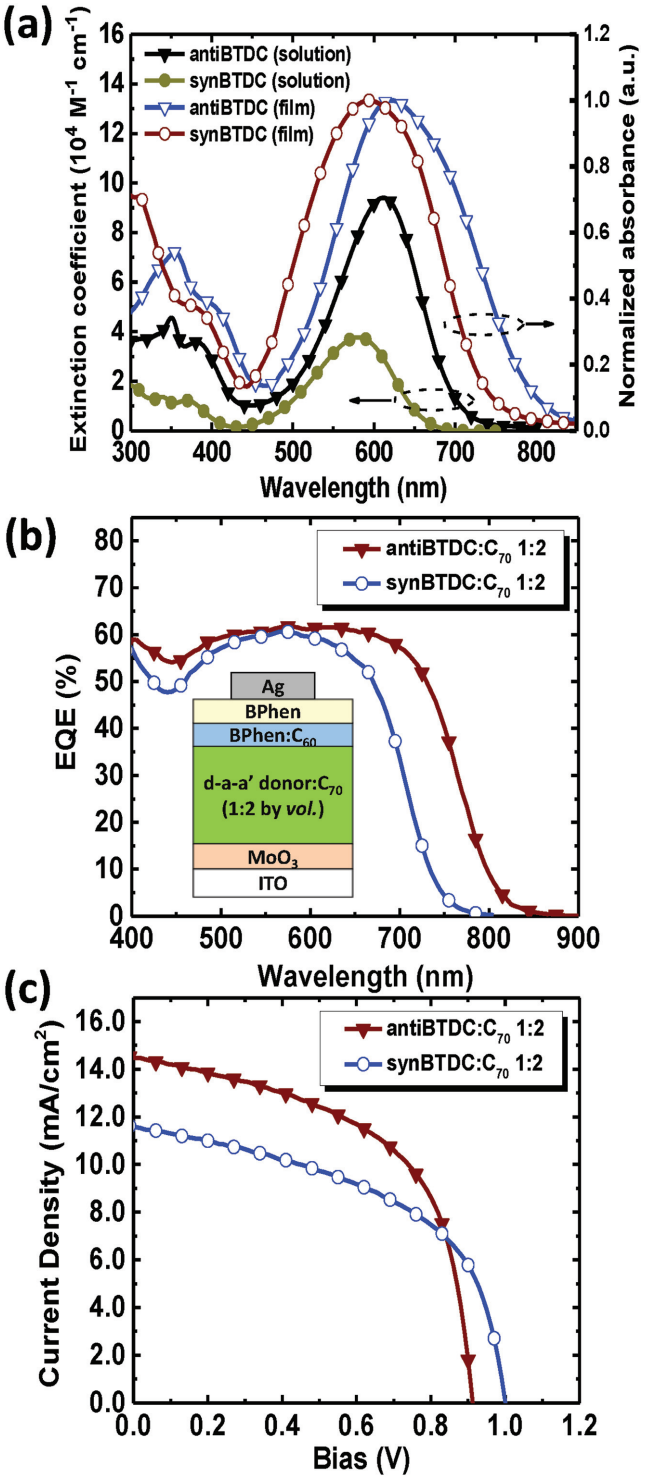

Figure 2. a) Extinction coefficients and normalized absorbances of vacuum-deposited thin films of antiBTDC and synBTDC as well as in dichloromethane solution. b) External quantum efficiency (EQE) spectra of antiBTDC:C_{70} and synBTDC:C_{70} organic photovoltaic cells. Inset: Device structure. c) Current-density–voltage (J–V) characteristics of devices in (b).

Table 1. Device performances of the d–a–a′ donor:C_{70} OPV cells.

Device	R_S [Ω cm^2]	J_{SC} [mA cm^{-2}]	V_{OC} [V]	FF	PCE [%]
antiBTDC:C_{70} (1:2, 60 nm)	1.42 ± 0.04	14.2 ± 0.7	0.91 ± 0.01	0.56 ± 0.01	7.2 ± 0.3
synBTDC:C_{70} (1:2, 50 nm)	1.86 ± 0.04	11.6 ± 0.6	1.01 ± 0.01	0.52 ± 0.01	6.1 ± 0.3
PYDC:C_{70} (1:2, 50 nm)	3.26 ± 0.07	10.1 ± 0.5	1.06 ± 0.01	0.48 ± 0.01	5.1 ± 0.2

Both antiBTDC and synBTDC are mixed with C_{70} with 1:2 ratio (see Table S5, Supporting Information, for device performance with different blend ratios) to achieve the highest PCE, with different optimized active layer thicknesses (60 and 50 nm thick, respectively). Atomic force microscopy (AFM) images of the d–a–a′ donor:C_{70} 1:2 mixtures are shown in Figure S5 (Supporting Information). The two films exhibit similar surface morphologies, although synBTDC:C_{70} shows a higher mean square roughness.

The external quantum efficiencies (EQE) versus wavelength of OPVs employing these two donors are shown in Figure 2b. The antiBTDC:C_{70} cell shows absorption extending to λ = 850 nm, while synBTDC:C_{70} cell is blue-shifted to λ = 800 nm. Figure 2c shows the fourth quadrant current-density–voltage (J–V) characteristics, with detailed device parameters listed in **Table 1**. The antiBTDC:C_{70} cell exhibits J_{SC} = 14.2 ± 0.7 mA cm^{-2}, V_{OC} = 0.91 ± 0.01 V, FF = 0.56 ± 0.01, and PCE = 7.2 ± 0.3% under 1 sun intensity, AM 1.5G simulated solar illumination. The cross-conjugated synBTDC has reduced performance compared to that of antiBTDC with J_{SC} = 11.6 ± 0.6 mA cm^{-2}, FF = 0.52 ± 0.01, and PCE = 6.1 ± 0.3%. However, the V_{OC} = 1.01 ± 0.01 V of the synBTDC-based device is 0.1 V higher than that of its antiBTDC-based counterpart due to the lower HOMO energy of the former.

Steady-state PL spectra of antiBTDC and synBTDC are shown in **Figure 3**a and Figure S6a (Supporting Information), respectively, along with their HOMO and LUMO energies relative to those of C_{70} (insets). The neat C_{70} emission spectrum is also depicted in Figure 3a for reference. When excited at λ = 442 nm, the antiBTDC film exhibits an NIR emission peak at λ = 870 nm, while the synBTDC film emits with the peak at λ = 800 nm. In both cases, the PL emission from the C_{70} blends is blue-shifted by ≈50 nm with several times higher intensity compared with the neat donor film. As we increase the antiBTDC:C_{70} blend ratio from 1:2 to 1:8, the emission is further blue-shifted and the intensity increases by more than ten times (Figure 3a). To understand this phenomenon, antiBTDC is diluted in poly(methyl methacrylate) (PMMA) with a 1:100 weight ratio to suppress intermolecular interactions. As shown in Figure 3b, the emission wavelength of the antiBTDC:PMMA film is 150 nm shorter as compared to that of the neat antiBTDC film along with two orders of magnitude higher intensity. Similarly, there is a 150 nm blue shift in the case of synBTDC:PMMA film emission (Figure S6b, Supporting Information).

The time-resolved transient PL of antiBTDC-based films blended with PMMA (1:100) and C_{70} (1:2), respectively, were examined and then fit to biexponential time decays as shown in Figure 3c. The time constants of antiBTDC:PMMA emission obtained from the fits are τ_{a1} = 40 ± 10 ps and τ_{a2} = 200 ± 20 ps, while the parameters for antiBTDC:C_{70} are τ_{b1} = 30 ± 10 ps and τ_{b2} = 120 ± 10 ps. The neat antiBTDC donor film, on the other hand, shows a single exponential time decay of τ_d = 190 ± 30 ps (Figure S7a, Supporting Information). Figure 3d and Figure S7b (Supporting Information) depict the transient emission of antiBTDC:PMMA and antiBTDC:C_{70} films at different wavelength intervals. The decay becomes slower at longer wavelengths. As indicated by the dashed line in Figure 3d, the antiBTDC:PMMA emission between λ = 790 and 880 nm has

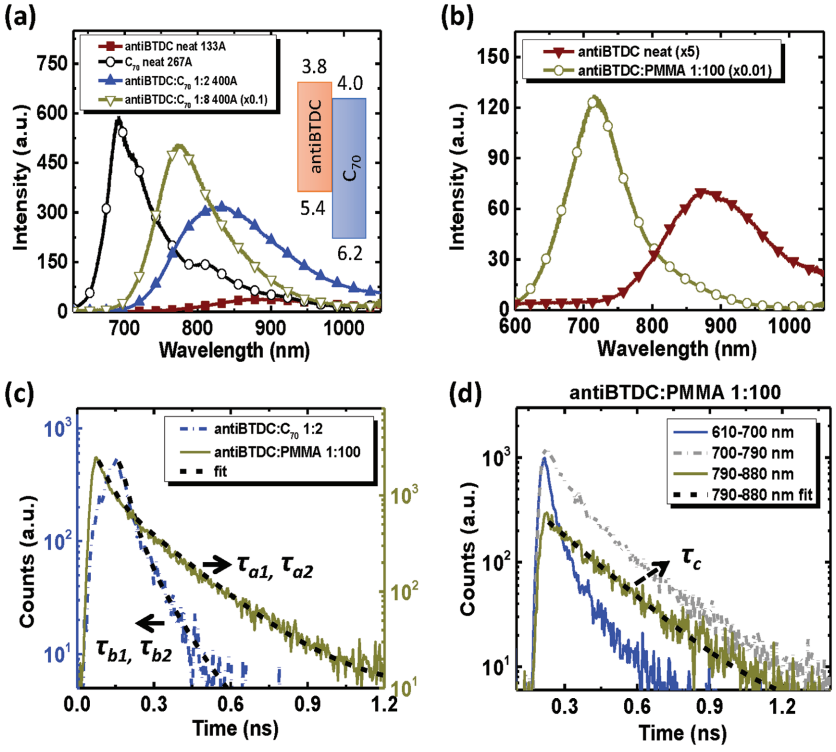

Figure 3. a) Steady-state photoluminescence (PL) spectra of antiBTDC neat donor, donor:C_{70} blends, and neat C_{70}. Inset: Energy level diagram of the antiBTDC donor relative to C_{70}. Numbers are energies of the frontier orbitals in eV. b) PL spectra of antiBTDC diluted in a poly(methyl methacrylate) (PMMA) matrix, and as a neat film. c) Time-resolved transient PL of antiBTDC:PMMA 1:100, and antiBTDC:C_{70} 1:2 blends. d) Wavelength-resolved transient PL of antiBTDC:PMMA. The time constants obtained from the fits (dashed lines) are: τ_{a1} = 40 ± 10 ps, τ_{a2} = 200 ± 20 ps; τ_{b1} = 30 ± 10 ps, τ_{b2} = 120 ± 10 ps; and τ_c = 210 ± 20 ps.

a single exciton lifetime of τ_c = 210 ± 20 ps. The films of synBTDC mixed with PMMA and C_{70} showed similar transient behaviors (see Figure S6c,d, Supporting Information).

Compared with previously reported DTP-based d–a–a′ molecules,[15] antiBTDC and synBTDC with fused coplanar aryl groups have reduced rotational disorder and thus improved π-stacking in the solid state. Furthermore, the electroactive carbon of the thiophene in the DTP donor unit is blocked by fusing a phenylene ring. The smaller BLA and shorter C1—C2 bond length of antiBTDC compared to those of synBTDC indicates a stronger electronic coupling between donor and acceptor units, which leads to a larger absorption oscillator strength and fewer changes in bond length upon photoexcitation. Thus, conjugation of the donor moiety in antiBTDC can facilitate π-electron delocalization and promote intramolecular charge transfer transitions, resulting in a tendency to form mesomeric structures of the BT unit.[24,25] For synBTDC, however, π-electron delocalization is suppressed over the molecular backbone due to cross-conjugation regardless of the presence of the highly electronegative N atom. The DFT calculations further confirm the electronic characteristics of these two molecules. We find that antiBTDC has a larger MO spatial overlap and μ_{tr}, leading to a higher electronic transition probability[26] and a larger oscillator strength associated with the $S_1 \leftarrow S_0$ transition. These results qualitatively agree with Figure 2a where the absorption of antiBTDC is red-shifted with a higher extinction coefficient when compared to synBTDC.

Due to intimate intermolecular π–π stacking, the thin film absorption spectra of both isomers are broadened and red-shifted compared with their solution spectra, as shown in Figure 2a. The antiparallel arrangement assembles into centrosymmetric π-stacked dimers, resulting in a net dipole moment of zero.[13,27] Compared with synBTDC, the closer stacking of antiBTDC results in stronger intermolecular π–π interactions that facilitate charge transport, and hence a higher film conductivity and fill factor.[28] Together with a smaller pitch angle, the molecular arrangement of antiBTDC shows a diminished molecular dipole indicated by its more homogeneous electron density distribution that further improves charge transport. Ultimately, with a more steeply tilted staircase-like packing habit and less efficient molecular dipole cancellation, the neat synBTDC shows ten times lower conductivity than antiBTDC as calculated from the SCLC measurement in Figure S4 (Supporting Information), which accounts for its higher device series resistance and hence lower FF than that of the antiBTDC:C_{70} cell. Additional shortening of the alkyl chains attached to the N atom of the electron-donating group can lead to closer intermolecular packing which promotes charge hopping and improved FF.[29]

The peak EQE of ≈60% for both antiBTDC:C_{70} and synBTDC:C_{70} cells indicates similar charge collection efficiencies, which implies that the differences in morphologies of the two blends are not critical to the differences in their current densities. The cross-conjugation of synBTDC results in reduced inter- and intramolecular charge transfer, and a larger energy gap compared with antiBTDC. Consequently, its HOMO level shifts to lower energy, thereby increasing V_{OC}. The lower efficiency of the synBTDC:C_{70} cell primarily resulting from the lower current density is therefore due to its absorption cutoff that does not extend as deeply into the NIR. The PCE = 6.1 ± 0.3%, however, is one of the highest efficiencies achieved among OPVs with V_{OC} > 1.0 V, which is advantageous for applications in high-voltage multijunction photovoltaic cells.[30,31]

Mixing of these compounds in the non-polar PMMA matrix eliminates solvation effects in the molecular emission spectra.[32] We therefore deduce that the hypsochromic shifts of the fluorescence in Figure 3b and Figure S6b (Supporting Information) of antiBTDC or synBTDC diluted in PMMA, respectively, are due to the emergence of monomer, in contrast to excimer emission in neat d–a–a′ thin films. The blue-shifted PL of the antiBTDC:C_{70} 1:8 blend compared with the 1:2 blend shown in Figure 3a suggests singlet emission with two possibilities: i) more pronounced antiBTDC monomer versus excimer emission as it is diluted in the blend or ii) direct emission from C_{70}. As seen from the energy level diagram in the insets of Figure 3a and Figure S6a (Supporting Information), the large differences in HOMO energies between antiBTDC or synBTDC and C_{70} facilitate efficient dissociation of excitons injected from the C_{70} side of the heterojunction. However, their similar LUMO energies with an offset smaller than 0.3 eV is insufficient to result in efficient exciton dissociation, causing back charge transfer to the d–a–a′ molecule followed by donor fluorescence. We conclude, therefore, that the singlet emission observed from the blends originates from the donor itself.

The transient PL further clarifies the origin of the spectral features in the PMMA and C_{70} blends. The antiBTDC:PMMA emission at λ = 790–880 nm corresponds to antiBTDC excimer fluorescence as observed in the neat antiBTDC film. It shows an exponential decay with the characteristic exciton lifetime of τ_c = 210 ± 20 ps (Figure 3d dashed line), which matches the τ_{a2} = 200 ± 20 ps obtained from the antiBTDC:PMMA transient PL. It is also nearly identical to the neat antiBTDC lifetime of τ_d = 190 ± 30 ps as shown in Figure S7a (Supporting Information). The emission from antiBTDC:PMMA therefore contains both monomer and excimer emission components, contributing to the shorter τ_{a1} and the longer τ_{a2}, respectively, in Figure 3c. The PL emission of antiBTDC:C_{70}, on the other hand, decays faster than antiBTDC:PMMA and is dominated by the shorter lifetime component of τ_{b1} = 30 ± 10 ps, very close to that for antiBTDC monomer emission, τ_{a1}. In Figure S7b (Supporting Information), we show the existence of long-wavelength emission with τ_e = 100 ± 20 ps, corresponding to τ_{b2} = 120 ± 10 ps in Figure 3c. It is due to both antiBTDC excimer (τ_{a2}) and CT state emission at the donor–acceptor interfaces (τ_{CT}), i.e., $\frac{1}{\tau_{b2}} = \frac{1}{\tau_{a2}} + \frac{1}{\tau_{CT}}$. Now τ_{b2} is $\approx \frac{1}{2}\tau_{a2}$, giving $\tau_{CT} \approx \tau_{a2} \approx 200$ ps. The emission intensities, however, are lower than the monomer donor emission even in the donor–acceptor blend.

The considerable donor emission from the donor:C_{70} blends suggests incomplete exciton dissociation at the donor–acceptor interfaces, with charge back-transferring to the donor molecule. This results in exciton dissociation within the donor domains, which reduces the cell shunt resistance (R_{sh}). Therefore, a linear increase of photocurrent under reverse bias is observed in the *J*–*V* characteristics in Figure 2b, resulting in $R_{sh} \approx 500\ \Omega\ cm^2$ and FF < 0.60.[33] A higher LUMO energy for more efficient

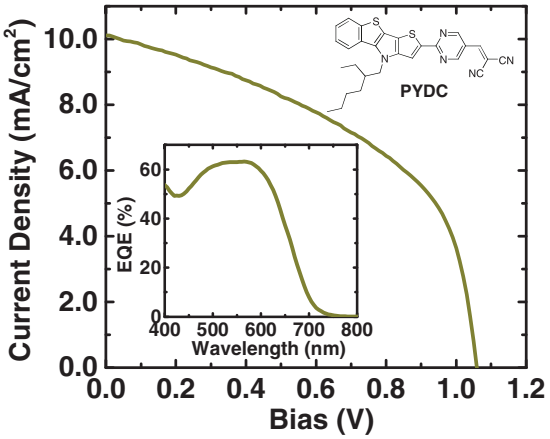

Figure 4. PYDC:C_{70} 1:2 organic photovoltaic cell *J–V* characteristics. *Inset*: Molecular structural formula of PYDC, and its *EQE* spectrum.

exciton dissociation is expected to improve the FF, although the current density may be reduced.

We have shown that the regioisomeric effects of antiBTDC and synBTDC determine, to a limited extent, V_{OC} of heterojunctions comprising C_{70}. To further examine the influence of molecular structure on V_{OC}, a d–a–a′ donor PYDC (see **Figure 4**, inset) was synthesized. In this molecule, the benzothiadiazole block in antiBTDC is replaced with a pyrimidine unit. Due to the reduced quinoidal character of pyrimidine, the absorption of PYDC shifts to shorter wavelengths with an onset at λ = 600 nm, indicating an increased optical energy gap of 2.05 ± 0.05 eV. The PYDC:C_{70} cell employs the same structure as antiBTDC:C_{70} and synBTDC:C_{70}, with an active layer thickness of 40 nm. The EQE spectrum and *J–V* characteristics are shown in Figure 4, with device parameters summarized in Table 1. The PYDC:C_{70} cell exhibits a relatively narrow absorption spectrum, leading to the lowest J_{SC} = 10.1 ± 0.7 mA cm^{-2} among the three donor molecules. However, with the central pyrimidine unit, the PYDC-based OPV achieves a higher V_{OC} = 1.06 ± 0.01 V, with FF = 0.48 ± 0.01 and PCE = 5.1 ± 0.2%. The series resistances (R_S) of the devices with different donors obtained from the *J–V* characteristics are also listed in Table 1, which accounts for the trends observed in FF; i.e., as R_S increases, FF decreases as expected.[34,35]

The heterotetracene-based d–a–a′ donors discussed above and the previously reported DTP-based d–a–a′ donor molecules[15] all contain a benzothiadiazole or pyrimidine central electron-withdrawing block, bridging the a′ unit of dicyanovinylene and an electron-donating aryl-substituted or benzene-fused DTP group. The molecular conjugation length (N) is defined as the number of double bonds along the shortest path connecting the terminal carbon atoms of the backbone,[36] that varies from 5 to 9 with the molecules we analyzed. **Figure 5**a summarizes the HOMO energies (E_{HOMO}) of these molecules as a function of 1/N. The molecules with benzothiadiazole are shown by solid squares, while those with pyrimidine are shown by open circles. Here, E_{HOMO} is chosen instead of commonly used electron transition energies since the conjugation length of both molecular groups is only adjusted by modifying their electron-donating unit that primarily affects the HOMO energy.

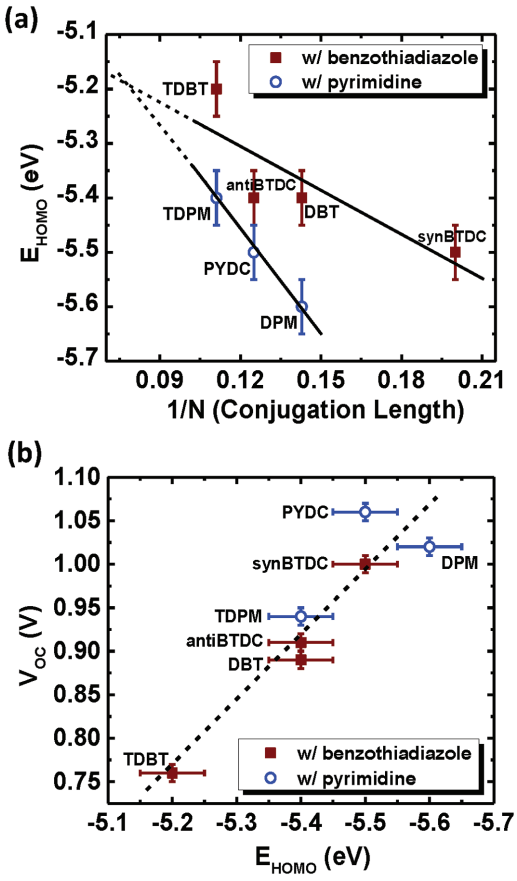

Figure 5. a) Highest occupied molecular orbital energy (E_{HOMO}) versus reciprocal of the backbone conjugation length (1/N) of a series of DTP- and heterotetracene-based d–a–a′ donor molecules. b) Open circuit voltage (V_{OC}) versus donor E_{HOMO} for d–a–a′:C_{70} heterojunctions.

An approximately linear relationship is observed between E_{HOMO} and 1/N that can be explained by the free electron model.[37] The longer conjugation (smaller 1/N) leads to more extended π-electron orbitals, resulting in red-shifted absorption and a shallower HOMO. With reduced quinoidal character, the molecules with pyrimidine generally exhibit larger energy gaps and deeper HOMO levels than their benzothiadiazole counterparts with the same N (PYDC-antiBTDC, DPM-DBT, TDPM-TDBT; for molecular structures see Figure S8, Supporting Information), and their HOMO levels are more sensitive to changes in conjugation, as indicated by the larger slope. The crossing point of the two fits at N = 13 (Figure 5a) indicates an upper limit of E_{HOMO} = −5.2 eV. Like polymers, extended molecules are subject to kinetically induced disruptions (e.g., twists or kinks) in the backbone, limiting the spatial extent of the orbitals in the excited state. Nevertheless, it is apparent that further tuning of the E_{HOMO} energy is possible for N > 9 reported here, which offers a design approach for achieving NIR absorbing donor molecules.

From Figure 5b, a deeper HOMO (i.e., smaller N) generally leads to an increased V_{OC}. The π-conjugation of antiBTDC is reduced compared with TDBT, with V_{OC} increased from 0.76 ± 0.01 to 0.91 ± 0.01 V. With a fused benzene ring on

the DBT molecule, antiBTDC achieves closer packing motifs than TDBT, resulting in a decreased transfer energy, and hence an increase in FF, from 0.46 ± 0.01 to 0.56 ± 0.01. Similar to antiBTDC, PYDC benefits from the improved molecular stacking over TDPM. It also achieves a higher V_{OC} = 1.06 ± 0.01 V. Further, DPM, with a relatively small N = 7, has the largest E_{HOMO} = −5.6 ± 0.05 eV of this group. However, the low FF = 0.33 ± 0.01 indicates poor charge transfer due to the unprotected electroactive carbon that limits V_{OC} compared with PYDC. The synBTDC-based device has V_{OC} = 1.01 ± 0.01 V, which is 0.1 V higher than antiBTDC and the smallest N = 5 achieved by interrupting the antiBTDC conjugation with the flipped thiophene unit within the molecular backbone. Such cross-conjugation effectively reduces the molecular conjugation and leads to a higher V_{OC}. Among all of the molecules discussed, the slope of the expected linear relationship[38] of V_{OC} to E_{HOMO} energy is 0.75 ± 0.13 C^{-1}, as indicated in Figure 5b.

The photon energy loss, E_{loss}, which is the difference between eV_{OC} and the photon energy, of the devices employing these donors is shown in Figure S9 (Supporting Information). The E_{loss} of the donors with benzothiadiazole central "a" unit all fall into the region between 0.6 and 0.8 eV, while the molecules with pyrimidine show E_{loss} between 0.8 and 1.0 eV. The antiBTDC and synBTDC exhibit E_{loss} < 0.7 eV, which is relatively small for organic solar cells.[39]

In conclusion, we have elucidated the structure–property–performance relationships of highly dipolar d–a–a′ small molecules used in organic donor–acceptor heterojunctions. Specifically, the molecules introduced with *anti* and *syn* asymmetric heteroacenes as coplanar donors of BTDC were used to investigate molecular regioisomeric effects on photogeneration efficiency when blended with fullerene acceptors. Both molecules pack in an antiparallel arrangement to achieve a centroymmetric dimer, leading to a net dipole moment of zero. The synBTDC with a shorter backbone conjugation length exhibits a reduced intra- and intermolecular charge transfer compared with antiBTDC. An optimized OPV based on antiBTDC:C_{70} blend achieves V_{OC} = 0.91 ± 0.01 V, FF = 0.56 ± 0.01, and PCE = 7.2 ± 0.3%. Despite the reduced charge transfer and blue-shifted absorption which lead to smaller J_{SC}, synBTDC shows a lower HOMO energy with higher V_{OC} = 1.01 ± 0.3 V, with a power conversion efficiency of 6.1 ± 0.3%. The design of PYDC leads to a further enhanced V_{OC} = 1.06 ± 0.01 V due to the reduced quinoidal character of pyrimidine. We find that the V_{OC} of the d–a–a′ donor:C_{70} devices is a function of the donor conjugation length: a reduction of backbone conjugation lowers the HOMO level for both groups of molecules with embedded benzothiadiazole or pyrimidine central "a" unit, leading to an enlarged donor–acceptor HOMO–LUMO gap and a larger V_{OC}. Shortening the alkyl chains, or raising their LUMO energy for more complete exciton dissociation may lead to further improvements in FF, and ultimately the device performance.

Experimental Section

Synthesis and characterization details for antiBTDC, synBTDC, and PYDC are shown in Scheme S1 (Supporting Information). The single crystals of antiBTDC and synBTDC for X-ray analysis were obtained from a bilayer (CH_3OH/CH_2Cl_2) solution. Other chemicals used were purchased from commercial suppliers: MoO_3 (Sigma Aldrich), BPhen (Lumtec), C_{60} (MER), C_{70} (SES Research), and Ag (Alfa Aesar). The antiBTDC, synBTDC, and PYDC were purified by column chromotagraphy, while C_{60} and C_{70} were purified by temperature-gradient sublimation before vacuum thermal evaporation (VTE) deposition. Cyclic voltammetry (CH Instruments, Inc. CH1619B) was performed using a three-electrode electrochemical cell with a glassy carbon working electrode, a Pt wire counter electrode, and an Ag/AgCl reference electrode. The absorption spectra of the dyes in solution were acquired using a Jasco V-670 spectrophotometer. The absorbances of the neat donor solid films were measured by UV–vis (Perkin Elmer 1050).

All DFT calculations were carried out with the GAUSSIAN09 package at the B3LYP/6-31G(d,p) level with the geometry of the molecules taken from the single crystal structure. Solvent effects were included in both DFT and time-dependent DFT (TD-DFT) calculations using the polarizable continuum model with the dielectric constant of dichloromethane. The ground-state (DFT) and first singlet excited-state (TD-DFT) geometries for all the species were fully optimized without symmetric constraints. The TD-DFT calculations show the vertical singlet excitations, oscillator strengths, and molecular orbital contributions to each singlet transition.

Organic photovoltaic devices were grown on pre-patterned indium tin oxide (ITO) coated glass substrates purchased from Lumtec, with sheet resistances of 15 Ω sq^{-1}. The substrate surface was detergent and solvent cleaned prior to deposition, followed by CO_2 snow cleaning[40] and exposure to ultraviolet–ozone for 10 min. The thin films were deposited in a high vacuum chamber with a base pressure of 10^{-7} Torr. The MoO_3, BPhen, and Ag films were deposited at 0.1 nm s^{-1}. The d–a–a′ donor:C_{70} (1:2) and BPhen:C_{60} (1:1) blends were co-deposited at 0.1 nm s^{-1}, with the rate of each material adjusted to achieve its volume ratio in the mixed layer. The deposition rates and thicknesses were measured using quartz crystal monitors and calibrated by variable-angle spectroscopic ellipsometry. The growth areas of organics and metals were defined by deposition through shadow masks, whereby the 2 mm^2 device area results from the overlap between the patterned ITO anode and the Ag cathode.

Following device fabrication, current-density–voltage (*J*–*V*) characteristics and spectrally resolved EQEs were measured in a glove box filled with ultra-pure N_2 (<0.1 ppm). A solar simulator provided AM 1.5G illumination (ASTM G173-03) whose 300 W Xe lamp intensity was calibrated with a National Renewable Energy Laboratory (NREL) traceable Si reference cell. The illumination intensity was adjusted using neutral density filters. A total of 16 devices on four patterned ITO substrates were fabricated during the same run for each donor material, with ≈75% yield. Errors quoted account for variations from three or more cells measured, as well as an additional systematic error of 5% for J_{SC} and PCE. Focused monochromatic light from a 150 W Xe lamp that under-filled the device area was used for measuring EQE. The OPV current from light chopped at 200 Hz was input to a lock-in amplifier. The responsivities of both the device and a NIST-traceable calibrated Si photodetector were compared to calculate EQE. The J_{SC} values listed in Table 1 are determined from the integrated EQE spectra, which are within ±5% compared with J_{SC} under 1 sun AM 1.5G illumination when corrected for spectral mismatch.[41]

The steady-state PL spectra were measured using a Si charge-coupled device (CCD) array (PIXIS:400) connected to a fiber-coupled monochromator (Princeton Instruments SP-2300i). The donor:poly(methyl methacrylate) (PMMA) films with 1:100 weight ratio used in PL measurements were prepared by dissolving the mixture in tetrahydrofuran (THF) before spin-coating onto Si substrates. The films were excited in vacuum by a He–Cd laser at a wavelength of λ = 442 nm, with spectra collected normal to the film plane. For time-resolved transient PL, samples grown on Si or quartz were excited at λ = 480 nm by a Ti:sapphire laser (Clark-MXR CPA-series) pumped optical parametric amplifier (TOPAS-C) using 150 fs pulses at 1 kHz repetition

rate. The spectra were obtained using a streak camera (Hamamatsu C4334).

Supporting Information

Supporting Information is available from the Wiley Online Library or from the author.

Acknowledgements

X.C. and C.-L.C. contributed equally to this work. This work was supported by the SunShot Program of the Department of Energy (X.C., experiment, analysis; S.R.F., analysis), the Air Force Office of Scientific Research (X.L., experiment, analysis; S.R.F., analysis), the Air Force Office of Asian Office of Aerospace R&D (FA2386-15-1-4030) (C.L.C, experiment, analysis; K.T.W., analysis), and the Ministry of Science and Technology (MOST), Taiwan (104-2113-M-002-006-MY3) (C.L.C, S.H.C., and I.H.L, experiment, analysis; K.T.W., analysis).

Received: April 12, 2016
Revised: June 6, 2016
Published online: July 25, 2016

[1] P. Peumans, S. Uchida, S. R. Forrest, *Nature* **2003**, *425*, 158.
[2] P. Peumans, A. Yakimov, S. R. Forrest, *J. Appl. Phys.* **2003**, *93*, 3693.
[3] B. P. Rand, J. Genoe, P. Heremans, J. Poortmans, *Prog. Photovoltaics Res. Appl.* **2007**, *15*, 659.
[4] A. Mishra, P. Bäuerle, *Angew. Chem., Int. Ed.* **2012**, *51*, 2020.
[5] Y. Lin, Y. Li, X. Zhan, *Chem. Soc. Rev.* **2012**, *41*, 4245.
[6] G. Wei, S. Wang, K. Renshaw, M. E. Thompson, S. R. Forrest, *ACS Nano* **2010**, *4*, 1927.
[7] X. Xiao, J. D. Zimmerman, B. E. Lassiter, K. J. Bergemann, S. R. Forrest, *Appl. Phys. Lett.* **2013**, *102*, 073302.
[8] X. Xiao, K. Bergemann, J. Zimmerman, K. Lee, S. Forrest, *Adv. Energy Mater.* **2013**, *4*, 1301557.
[9] G. Wei, X. Xiao, S. Wang, J. D. Zimmerman, K. Sun, V. V. Diev, M. E. Thompson, S. R. Forrest, *Nano Lett.* **2011**, *11*, 4261.
[10] L.-Y. Lin, Y.-H. Chen, Z.-Y. Huang, H.-W. Lin, S.-H. Chou, F. Lin, C.-W. Chen, Y.-H. Liu, K.-T. Wong, *J. Am. Chem. Soc.* **2011**, *133*, 15822.
[11] Y.-H. Chen, L.-Y. Lin, C.-W. Lu, F. Lin, Z.-Y. Huang, H.-W. Lin, P.-H. Wang, Y.-H. Liu, K.-T. Wong, J. Wen, D. J. Miller, S. B. Darling, *J. Am. Chem. Soc.* **2012**, *134*, 13616.
[12] S.-W. Chiu, L.-Y. Lin, H.-W. Lin, Y.-H. Chen, Z.-Y. Huang, Y.-T. Lin, F. Lin, Y.-H. Liu, K.-T. Wong, *Chem. Commun.* **2012**, *48*, 1857.
[13] O. L. Griffith, X. Liu, J. A. Amonoo, P. I. Djurovich, M. E. Thompson, P. F. Green, S. R. Forrest, *Phys. Rev. B* **2015**, *92*, 085404.
[14] X. Che, X. Xiao, J. D. Zimmerman, D. Fan, S. R. Forrest, *Adv. Energy Mater.* **2014**, *4*, 1400568.
[15] H.-I. Lu, C.-W. Lu, Y.-C. Lee, H.-W. Lin, L.-Y. Lin, F. Lin, J.-H. Chang, C.-I. Wu, K.-T. Wong, *Chem. Mater.* **2014**, *26*, 4361.
[16] N. F. Phelan, M. Orchin, *J. Chem. Educ.* **1968**, *45*, 633.
[17] X. Meng, G. Zhao, Q. Xu, Z. a. Tan, Z. Zhang, L. Jiang, C. Shu, C. Wang, Y. Li, *Adv. Funct. Mater.* **2014**, *24*, 158.
[18] M. Kertesz, C. H. Choi, S. Yang, *Chem. Rev.* **2005**, *105*, 3448.
[19] F. Meyers, S. R. Marder, B. M. Pierce, J. L. Bredas, *J. Am. Chem. Soc.* **1994**, *116*, 10703.
[20] A. Armin, G. Juska, M. Ullah, M. Velusamy, P. L. Burn, P. Meredith, A. Pivrikas, *Adv. Energy Mater.* **2014**, *4*, 1401221.
[21] G. Juška, N. Nekrašas, K. Genevičius, *J. Non-Cryst. Solids* **2012**, *358*, 748.
[22] N. Li, B. E. Lassiter, R. R. Lunt, G. Wei, S. R. Forrest, *Appl. Phys. Lett.* **2009**, *94*, 023307.
[23] A. N. Bartynski, C. Trinh, A. Panda, K. Bergemann, B. E. Lassiter, J. D. Zimmerman, S. R. Forrest, M. E. Thompson, *Nano Lett.* **2013**, *13*, 3315.
[24] J. Casado, T. M. Pappenfus, L. L. Miller, K. R. Mann, E. Ortí, P. M. Viruela, R. Pou-Amérigo, V. Hernández, J. T. L. Navarrete, *J. Am. Chem. Soc.* **2003**, *125*, 2524.
[25] C.-L. Pai, C.-L. Liu, W.-C. Chen, S. A. Jenekhe, *Polymer* **2006**, *47*, 699.
[26] C.-L. Chung, C.-Y. Chen, H.-W. Kang, H.-W. Lin, W.-L. Tsai, C.-C. Hsu, K.-T. Wong, *Org. Electron.* **2016**, *28*, 229.
[27] H. Bürckstümmer, E. V. Tulyakova, M. Deppisch, M. R. Lenze, N. M. Kronenberg, M. Gsänger, M. Stolte, K. Meerholz, F. Würthner, *Angew. Chem., Int. Ed.* **2011**, *50*, 11628.
[28] V. Coropceanu, J. Cornil, D. A. da Silva Filho, Y. Olivier, R. Silbey, J.-L. Brédas, *Chem. Rev.* **2007**, *107*, 926.
[29] J. Lee, A. R. Han, H. Yu, T. J. Shin, C. Yang, J. H. Oh, *J. Am. Chem. Soc.* **2013**, *135*, 9540.
[30] S. Sista, Z. Hong, L.-M. Chen, Y. Yang, *Energy Environ. Sci.* **2011**, *4*, 1606.
[31] T. Ameri, N. Li, C. J. Brabec, *Energy Environ. Sci.* **2013**, *6*, 2390.
[32] V. Bulović, R. Deshpande, M. E. Thompson, S. R. Forrest, *Chem. Phys. Lett.* **1999**, *308*, 317.
[33] C. K. Renshaw, J. D. Zimmerman, B. E. Lassiter, S. R. Forrest, *Phys. Rev. B* **2012**, *86*, 085324.
[34] J. D. Servaites, S. Yeganeh, T. J. Marks, M. A. Ratner, *Adv. Funct. Mater.* **2010**, *20*, 97.
[35] B. Qi, J. Wang, *Phys. Chem. Chem. Phys.* **2013**, *15*, 8972.
[36] J. Gierschner, J. Cornil, H. J. Egelhaaf, *Adv. Mater.* **2007**, *19*, 173.
[37] J. Torras, J. Casanovas, C. Alemán, *J. Phys. Chem. A* **2012**, *116*, 7571.
[38] N. C. Giebink, G. P. Wiederrecht, M. R. Wasielewski, S. R. Forrest, *Phys. Rev. B* **2010**, *82*, 155305.
[39] K. Kawashima, Y. Tamai, H. Ohkita, I. Osaka, K. Takimiya, *Nat. Commun.* **2015**.
[40] R. Sherman, J. Grob, W. Whitlock, *J. Vac. Sci. Technol., B* **1991**, *9*, 1970.
[41] C. H. Seaman, *Sol. Energy* **1982**, *29*, 291.